Surface Topography: Metrology and Properties

PAPER

CrossMark

Design and characterization of textured surfaces for applications in the food industry

G Lazzini[1], L Romoli[1], L Blunt[2] and L Gemini[3]

1. Department of Engineering and Architecture, University of Parma, Parco Area delleScienze 181/A, 43124 Parma, Italy
2. EPSRC HUB Advanced Metrology, School of Computing and Engineering, University of Huddersfield, Queensgate, Huddersfield HD1 3DH, United Kingdom
3. ALPhANOV, Institut d'Optique d'Aquitaine, Rue François Mitterand, 33400 Talence, France

E-mail: luca.romoli@unipr.it

Abstract

The aim of this work is to design, manufacture and characterize surface morphologies on AISI 316L stainless steel produced by a custom designed laser-texturing strategy. Surface textures were characterized at a micrometric dimension in terms of areal parameters compliant with ISO 25178, and correlations between these parameters and processing parameters (e.g. laser energy dose supplied to the material, repetition rate of the laser pulses and scanning velocity) were investigated. Preliminary efforts were devoted to the research of special requirements for surface morphology that, according to the commonly accepted research on the influence of surface roughness on cellular adhesion on surfaces, should discourage the formation of biofilms. The topographical characterization of the surfaces was performed with a coherence scanning interferometer. This approach showed that increasing doses of energy to the surfaces increased the global level of roughness as well as the surface complexity. Moreover, the behavior of the parameters S_{pk}, S_{vk} also indicates that, due to the ablation process, an increase in the energy dose causes an average increase in the height of the highest peaks and in the depth of the deepest dales. The study of the density of peaks S_{pd} showed that none of the surfaces analyzed here seem to perfectly match the conditions dictated by the theories on cellular adhesion to confer anti-biofouling properties. However, this result seems to be mainly due to the limits of the resolving power of coherence scanning interferometry, which does not allow the resolution of sub-micrometric features which could be crucial in the prevention of cellular attachment.

Nomenclature

Symbol	Name	Unity of measure
RR	Laser repetition rate	kHz
ν	Scanning speed	mm s^{-1}
HOL	Horizontal overlap	dimensionless
H	Hatch distance	mm
F	Laser fluence	J cm^{-2}
N	Number of scans	dimensionless
E	Energy dose	J cm^{-2}
S_a	Average roughness	μm
S_q	RMS roughness	μm
S_{sk}	Skewness	dimensionless
S_{dr}	Developed interfacial area ratio	dimensionless
S_{pd}	Density of peaks	μm^{-2}
S_k	Core roughness	μm
Spk	Reduced peak height	μm
Svk	Reduced valley depth	μm
S_z	Maximum height	μm

1. Introduction

There are several examples of surface nano and micro structures with diverse properties that exist in nature [1–4]. The self-cleaning effect of lotus leaves, the adhesion of gecko's feet, the antireflectivity of moth eyes and the antifouling properties of fish scales are well known examples of such natural phenomena. As a result of these unique surface properties, there has been growing interest in biological interfaces and their unique features, and this has encouraged scientists and engineers to investigate the physico-chemical nature of such surface structures. The ultimate goal of this biomimetic surface research is the realization of synthetic surfaces reproducing the physico-chemical properties observed in living systems that could potentially be implemented in technological applications [5]. The ability to prevent the formation of biofilm is amongst the most reproducible features of biological interfaces. Synthetic interfaces with these properties have already gained relevance in numerous technological applications. Among these, one of the most relevant is the food industry. In particular, the formation of biofilms on the surface of food machinery can compromise food hygiene because biofilms often contain spoilage or pathogenic bacteria that can be dangerous to human health. In addition, the presence of biofilm on surfaces across food plants can seriously limit the process yield; for example, the occurrence of biofilms can increase the frequency of plant shut down for cleaning, it can reduce heat transfer and operating efficiency in heat exchange equipment, and can even increase frictional resistance and corrosion rates on surfaces, leading to high losses of energy and the spoiling of food stuffs [6–8].

Many unique properties of bio surfaces are correlated with the presence of surface micro- and/or nanostructures [5, 9, 10]. Numerous techniques have been explored with respect to the production of bio inspired large area topographies, which have included photolithography [11, 12], nanoprinting [13, 14], and electron beam lithography [15, 16]. These techniques offer the possibility of realizing structures with well-defined geometries repeated periodically on a workpiece surface. Consequently, such textures are completely identified by a relatively small number of simple geometrical parameters, such as the size and period of the repeating unit. These regular structures are useful for studying the correlations between the macroscopic properties and the surface morphology [11]. However, despite their excellent performance, these approaches suffer from some shortcomings, such as complexity (multiple processing steps), the need for expensive masks, the high process cost and slowness of the patterning process [10]. Recently, novel powerful approaches for the realization of biomimetic interfaces have been developed that combine the effectiveness of functional surface topographies with the possibility of functionalizing large areas, making them more suitable

for up-scaling to production environments. These techniques cover anodization [17], polymer film roughening [18, 19], electroerosion [20], and sol-gel processes [21, 22]. In particular, laser machining has emerged as a novel and promising approach for the high-speed modification of interfacial properties; in fact, this technique, especially with ultrashort laser pulses, can facilitate the realization of surface textures on a multi-dimensional scale, similar to those found in natural biological systems, in only a one-step process [23–25]. Moreover, these textures can be realized without the need for clean room facilities and can be implemented in different gaseous atmospheres with the additional possibility of controlling, to some degree, the surface chemistry [10]. This technique leads to surface topographies characterized by a random distribution of hills and dales (ISO 25178). This fact, often accompanied by inhomogeneities in the chemical composition, leads to a difficult correlation between the topographic features and the macroscopic properties of interest. Therefore, an accurate description of the geometry of such random topographies requires the use of statistical quantities related to the distribution of the surface topgraphical features of the processed area. The need for a complete description of surface roughness has led to the development of areal surface roughness parameters and their adoption into standards (ISO 25178) [26, 27]. Unfortunately, despite this new approach to surface characterization, the majority of the literature concerning the metrological characterization of biomimetic interfaces restricts the analysis to a few metrological quantities, such as the so-called average roughness (S_a) or the RMS roughness (S_q). This kind of description is not sufficient for a complete geometrical characterization of the topography, since it is known that surfaces with the same parameter values can have different geometries in terms of spatial properties and spatial frequency, and this consequently has a great effect on the surface functional properties [28, 29]. Therefore, efforts should be devoted to the introduction of more representative parameters from the ISO 25178 'toolbox' to give a more refined description of complex textures.

In this work, the surface roughness of AISI316L stainless steel samples treated with ultrashort laser pulses has been characterized in order to provide examples of surfaces that can be investigated for their anti-biofouling properties. AISI 316L austenitic stainless steel is widely used in the food industry because of its high resistance to corrosion by food products and detergents [30]. Several attempts have been made to correlate the occurrence of biofilm with the surface roughness of such stainless steel. Despite the examination into the relationship between the level of hygiene and the type of finishing, the published results are somehow contradictory [30, 31]. For example, many studies attribute the improved hygienic properties of certain finishes to the low average roughness R_a [32], while in other studies no clear relationship has been

found between the amount of biofilm and average roughness R_a [34].

The present study extends the use of areal surface parameters and metrological surface parameters to include those falling within the scope of standard ISO 25178. The parameters have been deployed in the reported work in order to assess the correlation between surface roughness and processing conditions, i.e. the laser energy dose supplied to the target. The list of roughness parameters includes average roughness S_a, RMS roughness S_q, skewness S_{sk}, developed interfacial area ratio S_{dr}, density of peaks S_{pd}, core roughness S_k, reduced valley depth S_{vk} and reduced peak height S_{pk}. A metrological analysis has been performed from topographical maps obtained using a coherence scanning interferometer, measuring at or just below micrometric resolution. The present reported work assessing optimal requirements for anti-biofouling has been conducted within the framework of the basic theories concerning the influence of surface roughness on bacterial adhesion. Finally, guidelines for the design of surfaces minimizing the nesting of microorganisms on stainless steel surfaces are derived and reported.

2. Requirements for the design of anti-biofouling surfaces

With regards to the relation between surface roughness and the formation of biofilm, several theories and mechanisms of adhesion have been proposed. First of all, a cell can be characterized as an external wall with a certain degree of elasticity. Several works in the literature show that the elastic modulus and non-covalent interactions between a surface and cell contribute decisively to the adhesive strength [35–37]. In the formation of a biofilm, the cell wall can change its shape up to a certain limit in order to adapt itself to the substrate geometry. Therefore, cells tend to adhere preferentially to surfaces that minimize the deformation of the cell itself, such as surfaces with favourably sized valleys or grooves. These surface features are also supposed to protect the cell against hydrodynamic turbulences [29, 35–39]. For example, Verran *et al* showed that in samples with a substrate of PMMA with an average roughness of 1.96 μm, *Candida albicans* adhere preferentially into defects, i.e. scratches [37, 40]. Whitehead *et al* observed the same behaviour for *Staphylococcus aureus* and *Pseudomonas aeruginosa* on Si surfaces coated with Ti characterized by pits with diameters ranging from '*fractions of μm to 2 μm*' [41].

In an attempt to adapt the cell curvature to a surface, the base cellular shape could play a crucial role. In particular, one can expect that cells, such as coccoid bacteria, with an almost spherically symmetrical shape, could adapt their surface curvature to a larger variety of rough patterns than cells, such as *Pseudomonas* bacteria that have a rod-like shape, i.e. an almost cylindrical symmetry. Cellular adhesion on surfaces is, in princi-

ple, influenced not only by the geometrical characteristic of cells, but also by other factors, such as the ability to secrete polymeric substances that facilitate the attachment, and experimental results that have been published over the years seem to confirm this hypothesis. For example, Ivanova *et al* showed that spherical *S. aureus* cells adhere more easily on molecularly smooth Ti surfaces compared to the rod-like *P. aeruginosa* [42]. They attribute this effect not only to the shape of the bacteria, but also to the more flexible cell membrane in *S. aureus* than in *P. aeruginosa*. As a result, *S. aureus* can adhere easily on a surface with spikes, whose spacing dimension is lower than the cellular size, by adapting its outer structure to the surface curvature. In these and other examples [23, 42–44], the emerging common concept is that the bacterial dimension defines a critical length-scale for bacterial adhesion—structures smaller than the cellular dimension have a negligible effect on bacterial attachment. This idea explains some conventions that have been introduced in the design of surfaces utilised in the food industry, for example, the rule that hygenic steel surfaces must have an average roughness lower than 0.8 μm dictated by the EHEDG (European Hygienic Equipment Design Group) and, additionally, the requirement of R_a to be less than 1.6 μm, dictated by the ISO 4287 standard for cleanability [31, 37]. Finally, the idea of a 'cutoff' threshold length scale of 0.2 μm for the formation of bacterial plaque on dental surfaces is proposed by Bollen *et al* [45]. To clarify this point, the authors report the argument proposed by Scardino *et al* [46], who studied the attachment of diatom cells of different sizes on polymide surfaces with grooves modeled from the fouling resistant bivalves *Mytilus galloprovincialis* and *Tellina plicata*. They found that for groove widths near the cell size, the number of adhered cells decreases significantly. The schematic diagram used to explain this behaviour is shown in figure 1. A cell standing on a surface whose roughness is larger than the cell size (figure 1(a)) adheres on the surface with a relatively large number of attachment points. In contrast, a surface whose roughness is smaller than the cell size provides a small number of attachment points, thus making cellular adhesion more difficult (figure 1(b)).

According to the hypotheses defined so far, and taking into account the fact that the average surface roughness S_a obtained by conventional machining ranges between 3.2–1 μm, the most frequent condition when generating surface texture by mechanical tools is that represented in figure 1(a); the alternation of peaks and valleys would create a favourable condition to host microorganisms. Therefore, the main idea is to look for a technological process which enables the production of multiscale hierarchical structures in which nanoscale features are superimposed on the microscale roughness. With these surface morphologies, the condition that minimizes the number of contact points depicted in figure 1(b) should be present across the surface, including the inclined flanks of
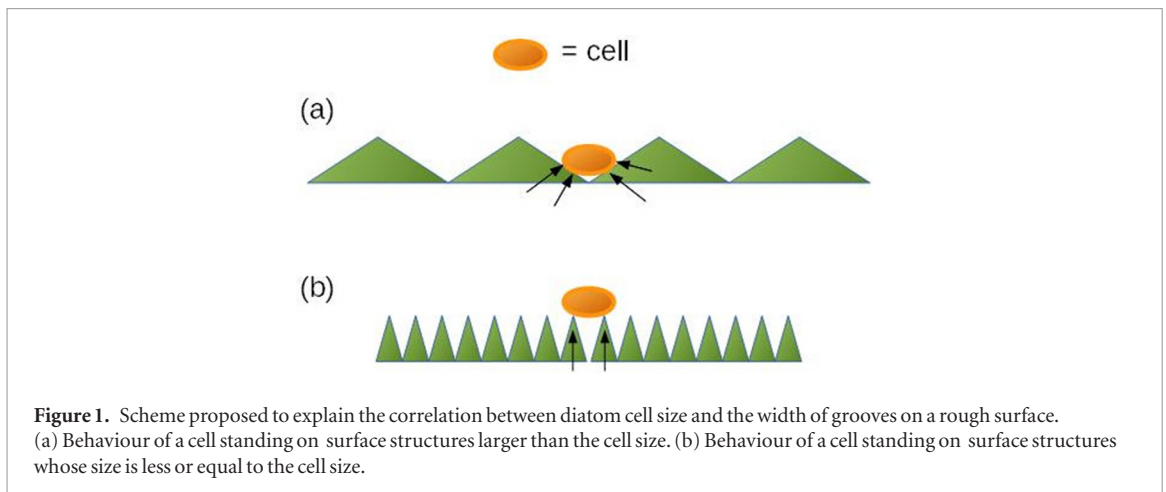
Figure 1. Scheme proposed to explain the correlation between diatom cell size and the width of grooves on a rough surface. (a) Behaviour of a cell standing on surface structures larger than the cell size. (b) Behaviour of a cell standing on surface structures whose size is less or equal to the cell size.
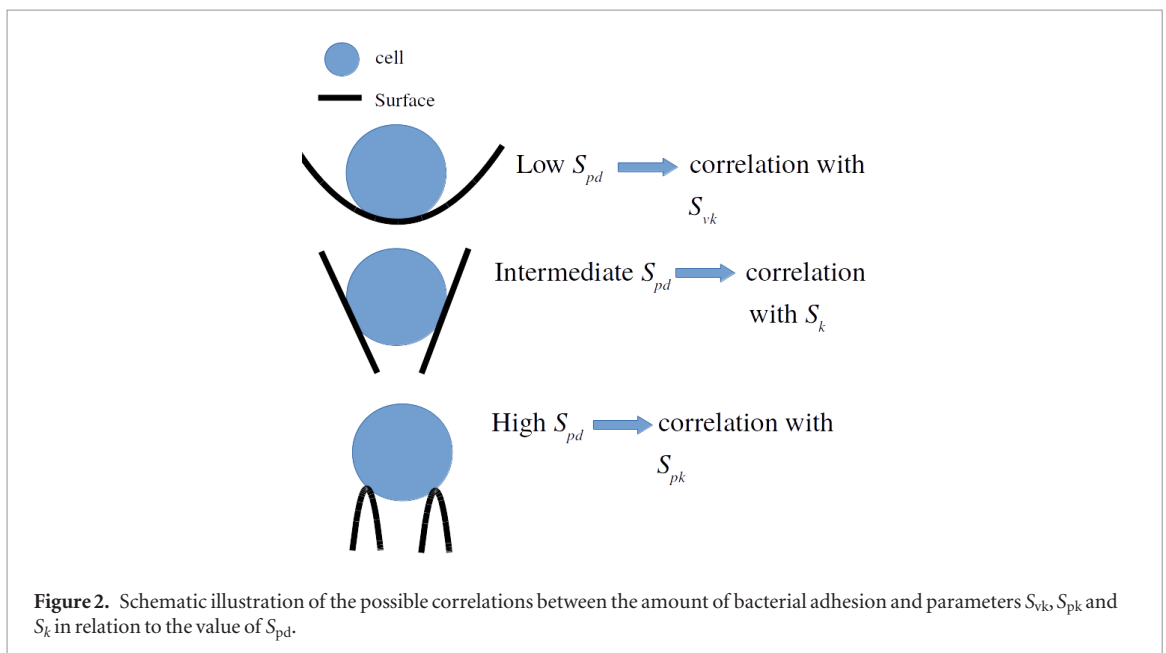

Figure 2. Schematic illustration of the possible correlations between the amount of bacterial adhesion and parameters S_{vk}, S_{pk} and S_k in relation to the value of S_{pd}.

the primary roughness. It should be noted that defining optimal attachment criteria by S_a values alone is essentially flawed as S_a refers only to surface amplitude information and does not infer spatial properties. In fact, two surfaces with differing roughnesses (S_a) could have identical spatial properties. A better quantifying parameter would be a roughness parameter based on spatial information such as peak density S_{pd} combined with a parameter inferring amplitude properties.

In order to define the number of peaks per area unit for an ideal surface to hinder the multiplication of the contact point between the bacteria and the surface, the attachment behaviour of *S. aureus*, which is represented as a blue circle in figure 2, was investigated. A single cell of this bacterium has an approximately spherical shape, whose diameter d is in the range 0.5–0.7 μm. Hence a critical value of the density of the peaks S_{pd} can be defined, which corresponds to a distance between adjacent peaks equal to the cellular diameter. This value is such that $(1/S_{pd})^{1/2} \approx d$, and it is equal to $S_{pd}^{crit} \approx 4 \ \mu m^{-2}$. For S_{pd} such that $S_{pd} < S_{pd}^{crit}$, we can expect that, for the most part, bacterial cells will stand

on the bottom of valleys, thus maximizing the contact area. In addition, since the reduced valley depth S_{vk} (see the appendix for the formal definition) is related to the surface depth in the bottom of the dales, one can expect a correlation between the amount of biofilm and S_{vk}. For high S_{pd}, i.e. such that $S_{pd} > S_{pd}^{crit}$, the bacteria will remain in contact with the peaks. Therefore, in an attempt to prevent the formation of biofilm, this situation must be considered preferable. By definition, the reduced peak height parameter S_{pk} should be correlated with the surface height above the mean plane. Therefore, for $S_{pd} > S_{pd}^{crit}$, we can expect a strong correlation between this parameter and the amount of biofilm. Finally, for intermediate values of peak density S_{pd}, it can be expected that a significant part of the cell surfaces will stand in contact with the sample surface at intermediate heights with respect to the mean height line. Consequently, it can be surmised that there should be a correlation between the amount of biofilm and the core roughness S_k, that, according to its definition, is related to the core height of the surface. However, it is important to emphasize that, at the moment,

Table 1. Process parameters and range of variation. The scan speed was varied according to the repetition rate to keep the overlap constant at 92%.

	Value/Range
Wavelength	1030 nm
Pulse duration	350 fs
Repetition rate, *RR*	100, 250, 500, 1000 kHz
Spot diameter	25 μm
Pulse overlap, HOL	92%
Scan speed, *v*	200, 500, 1000, 2000 mm s^{-1}
Hatch distance, *H*	5 μm
Laser fluence, *F*	0.36, 0.48, 0.69, 0.86, 1.14, 1.35, 1.69, 1.94, 2.33 J cm^{-2}
Number of scans, *N*	10
Energy dose, *E*	178, 235, 340, 423, 560, 663, 831, 950, 1143 J cm^{-2}

these arguments are only hypothetical and do not account for additional effects, such as disomogeneities in the chemical composition from the summit to the valleys, bacterial motility, the dynamics of the fluid containing the bacteria, etc. Therefore, these theories need to be investigated experimentally.

3. Materials and laser processing

In order to assess the optimal surface topographies for antifouling, a series of irradiated samples consisting of square plates of 50 mm side and a thickness of 2 mm, made of AISI 316L stainless steel, were examined. AISI 316L was chosen as the target material as it is widely employed in food handling and food processing. All the samples had a baseline as-received average roughness of $S_a < 0.5$ μm. Before the laser treatment, the samples were cleaned for 5 min in acetone in an ultrasound bath. Following this, laser texturing was performed without shielding gas. Textured surfaces with dimensions of 8×8 mm^2 were obtained by irradiation with linearly horizontally polarized pulses of an Amplitude Systems Satsuma HP3 laser system with an average power up to 40 W. The repetition ranged up to 1 MHz, the central wavelength was 1030 nm and the pulse duration was 350 fs. The laser beam was firstly magnified by a factor of three through a beam expander and then directed into a scanning system to provide accurate positioning of the laser pulses. The final focus was achieved using a 100 mm *f*-theta lens to a spot diameter of approximately 25 μm. The laser pulse repetition rate, *RR* and scan speed are indicated below. Four different experimental conditions were examined: $RR = 100$ kHz and $v = 200$ mm s^{-1}, $RR = 250$ kHz and $v = 500$ mm s^{-1}, $RR = 500$ kHz and $v = 1000$ mm s^{-1}, and finally $RR = 1000$ kHz and $v = 2000$ mm s^{-1}. The horizontal overlap HOL is defined as:

$$\mathrm{HOL} = \frac{d-l}{d} \times 100 \qquad (1)$$

where *d* is the beam diameter and *l* is the length of the path made by the laser source between two consecutive

pulses ($l = v/RR$). The processing conditions specified above were set to maintain the horizontal overlap at 92% in order to maximize the efficiency of the laser ablation. For each combination of scan speed and repetition rate, nine values of laser fluence *F* (defined as the ratio between the pulse energy and the focused spot area) were chosen, ranging from 0.36–2.33 J cm^{-2}. The selected range of *F* was established based on a lower limit necessary to overcome the specific modification threshold of the material and an upper limit to avoid thermal damage and surface melting. A factorial experimental design was then developed with 4 levels of repetition rate and 9 levels of fluence, giving a total of 36 textured surfaces.

The energy dose, *E*, was defined as the ratio between the total energy supplied to the surface by the radiation and the total irradiated area. Higher energy dose regimes could also potentially be achieved by superimposing multiple successive scans, *N*. In particular, for this experiment, the same process was repeated for $N = 10$ scans. Therefore, by neglecting the thermal losses between two consecutive scans, the total energy dose supplied to the surfaces ranged from 178–1143 J cm^{-2}. Prior to surface characterization, the treated surfaces were immersed in an ultrasonic bath for 10 min using ethanol at room temperature. They were then washed with fresh ethanol and finally dried in vacuum at room temperature.

For the sake of clarity, table 1 summarizes the process parameters used for the tests together with other process variables which were kept constant in the present study.

4. Surface characterization

The surfaces were first inspected from a qualitative point of view using a Phenom desktop scanning electron microscope (SEM). This was done with the objective of ascertaining the presence of hierarchical structures by using the maximum allowed depth of focus of the SEM at a magnification up to 6000×. The topography of the surfaces was quantified using a coherence scanning interferometer. The experimental apparatus employed was the Taylor-Hobson CCI MP.
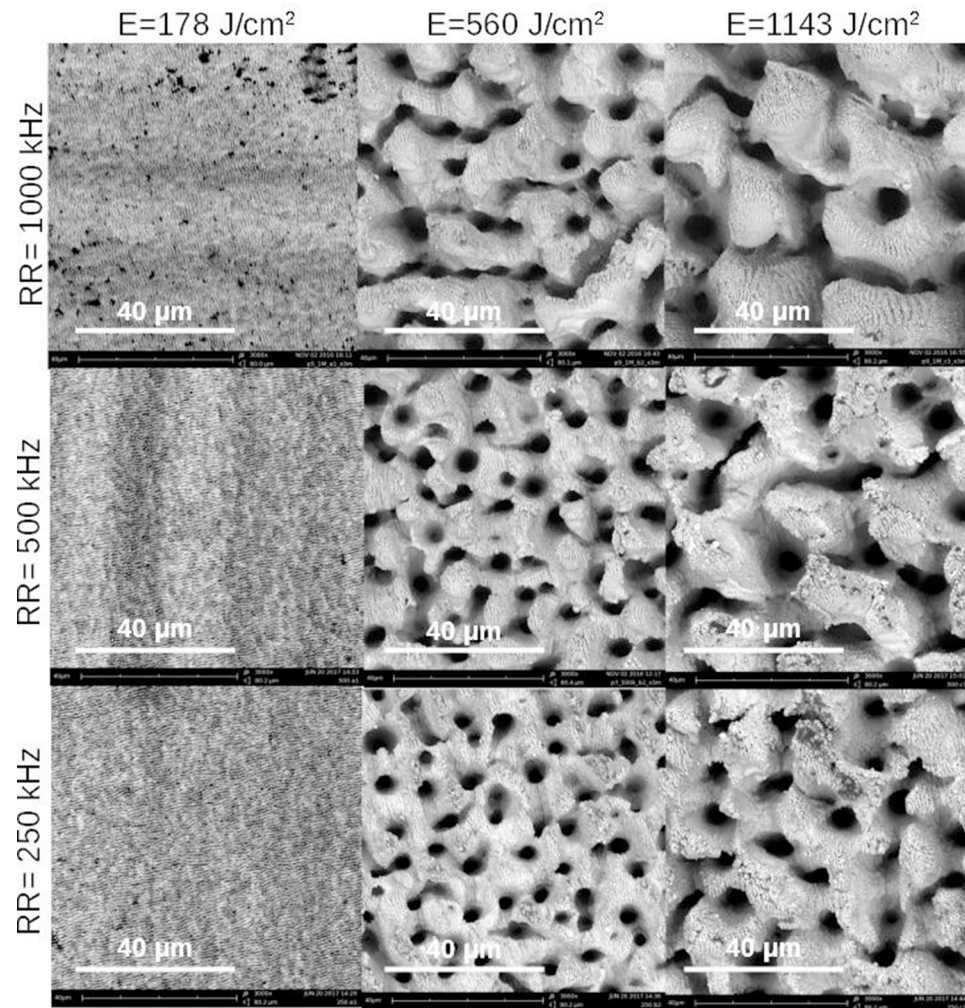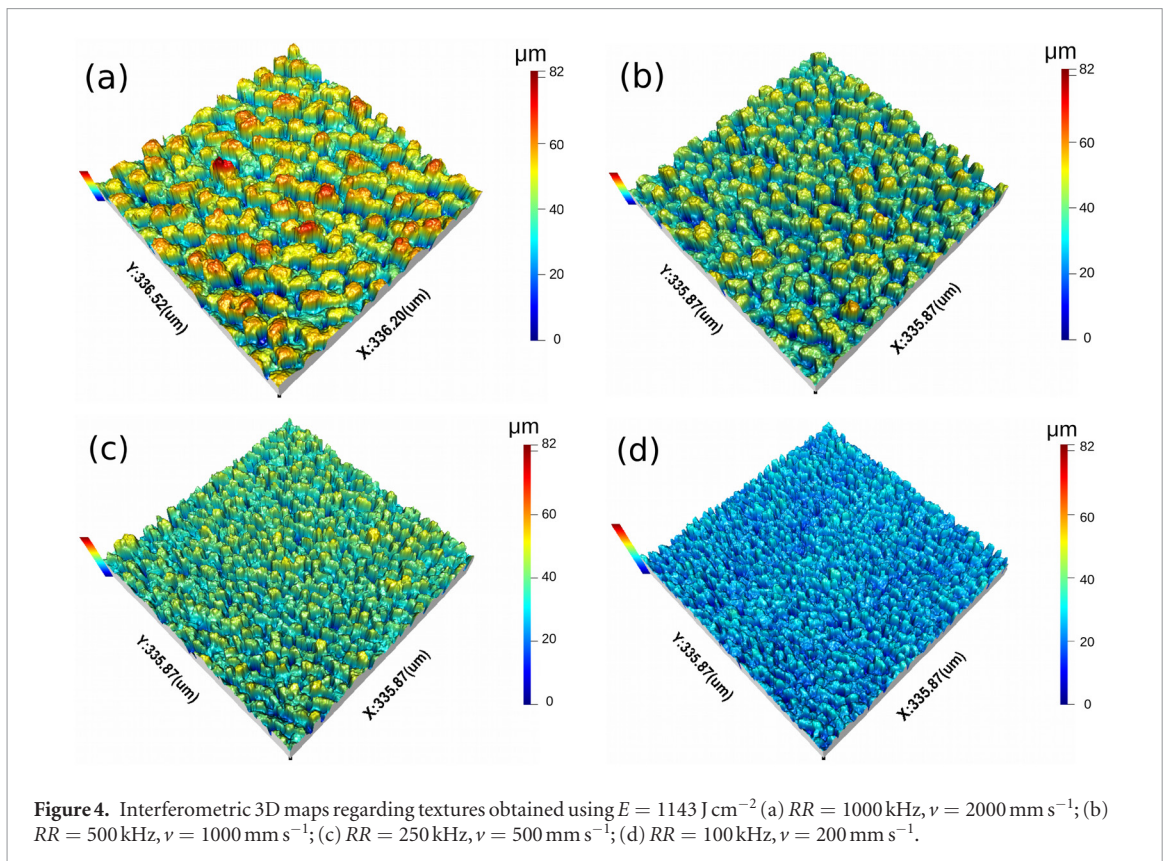
Figure 3. SEM images of the laser-ablated surfaces obtained with different values of *RR* (on the left) and for growing values of *E* (on the top) supplied to the samples.

A 50× objective was used with a numerical aperture of 0.55 and a working distance of 3.4 mm. The maximum measurement area was a square size of 336×336 μm^2 where the optical lateral resolving power of the objective was limited to 0.4 μm, and the acquisition software can produce digital maps with a maximum size of 1024×1024 resulting from interpolation procedures. Therefore, the effective resolving power can reach nominal values of approximately 338 nm. A problem concerning the data acquisition with coherence scanning interferometry is related to the fact that, with the numerical aperture specified, the apparatus cannot detect signals originating from surfaces whose slopes are greater than 27.5°. This is because the light is scattered from the slopes away from the acceptance cone of the objective. This drawback results in the presence of non-measured points in the digital maps. To limit this problem, a data binning protocol was applied to the acquired matrices, reducing the size of the maps to 512×512. This level of binning is a reasonable compromise between the need to minimize the number of non-measured points and the need to minimize the number of optical artifacts in the form of non-physical peaks.

The interferometric maps were first subjected to a spline interpolation procedure, whose aim was to 'fill in' the non-measured points resulting from the finite acceptance angle of the objective. The calculation of metrological parameters was performed on previously filtered digital maps. The filtering procedure included a least squares leveling operation and a Gaussian *S*-filter with a cutoff wavelength of 2.1 μm on both the *x* and *y* directions. The purpose of the filtering procedure was to cut off the noise observed mainly in the maps obtained with low energy doses. The procedures which followed for the calculation of the roughness parameters described in this work are explained in detail in the appendix.

5. Results and discussion

In figure 3, a series of SEM images of the portions of surfaces obtained with different values of *RR* and *v* and for growing values of *E* supplied to the samples is reported. At low *E*, laser-induced periodic surface structures (LIPSS) called LSFL (low spatial frequency LIPSS) are observed. These structures are oriented perpendicularly to the laser polarization with a period

Figure 4. Interferometric 3D maps regarding textures obtained using $E = 1143 \, J \, cm^{-2}$ (a) $RR = 1000 \, kHz$, $v = 2000 \, mm \, s^{-1}$; (b) $RR = 500 \, kHz$, $v = 1000 \, mm \, s^{-1}$; (c) $RR = 250 \, kHz$, $v = 500 \, mm \, s^{-1}$; (d) $RR = 100 \, kHz$, $v = 200 \, mm \, s^{-1}$.

comparable to the laser wavelength. The presence of LSFL with similar conditions of irradiation has been previously assessed in other works in the literature [47–50].

By increasing parameter E, LIPSS are replaced with columnar structures whose transversal dimensions increase with increasing E. In addition, it is possible to distinguish periodic features situated on the top of such columnar structures. SEM images obtained at higher resolutions than those shown in figure 3 reveal that these periodic features have a period comparable with the laser wavelength. Another interesting feature concerning the experimental conditions with which the laser texturing has been performed is the variation of the surface morphology with the RR for a given value of energy dose E. In particular, by fixing E, a decrease in RR seems to reduce the transversal dimension of the columnar structures.

Several physical phenomena are expected to contribute to the morphologies observed. First of all, at lower energy doses, Marangoni convection, driven by the high thermal gradients generated by ultrafast laser–matter interaction, has been proposed as the dominant physical process that occurs [51]. At higher E, the common idea is that the surface morphology is the result of a modulated energy deposition due to the interference between the laser pulses and surface plasmon polaritons (SPP). By further increasing the E parameter, the carrier densities reach values for which the formation of SPPs can no longer occur. In this situation, the dominant mechanisms that control the surface morphology change and a transition from LIPSS to bumps is observed.

A decrease in the spike width for decreasing values of RR is confirmed by a qualitative analysis of the interferometric maps reported in figure 4. In addition, as noted in the vertical scales of these maps, we observe that a decrease in the repetition rate also determines a decrease in the height of the surface structures.

In figures 5 and 6, a plot of the average roughness S_a and RMS roughness S_q versus the energy dose E is shown. The two graphs show that S_a and S_q increase almost linearly with E, indicating that the increase in the transversal size with E shown in figure 3 is accompained by an increase in the average height. The slope of the linear dependence decreases for decreasing values of the repetition rate.

While the correlation expressed in figures 5 and 6 is quite well defined, the correlation between E and the skewness S_{sk} (figure 7) is less evident. However, some interesting conclusions can be drawn by observing this last parameter. S_{sk} seems to be almost constant or weakly decreasing as a function of E for all the experimental conditions. According to the definition of S_{sk} [52], the decrease of S_{sk} for decreasing values of RR means that the surface is increasingly valley dominated. This increasingly negative value will be self limiting and then reverse when the so-called valleys grow in lateral extent to a point where the calculated mean plane shifts downwards. This effect is due to the ablation of material that, according to the qualitative observations made on the interferometric maps, is more effective for low values of RR and v where the valley features are relatively isolated compared to the surrounding topography [53].
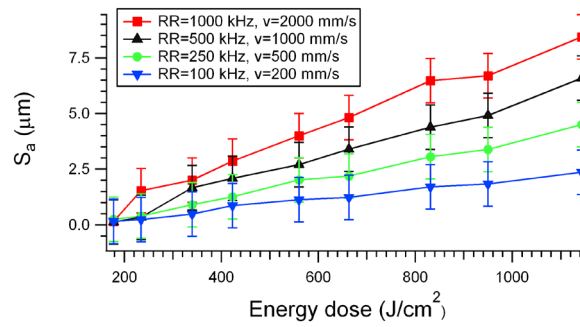
Figure 5. Evolution of the average roughness S_a with energy dose E for ultrashort laser-textured surfaces (evaluation area: $336 \times 336 \ \mu\text{m}^2$). The error bars associated with the values of E are the same size as the markers (standard deviation).
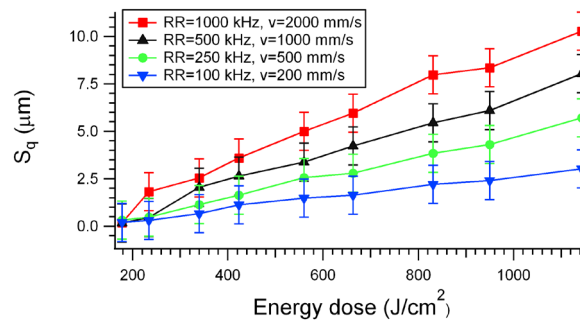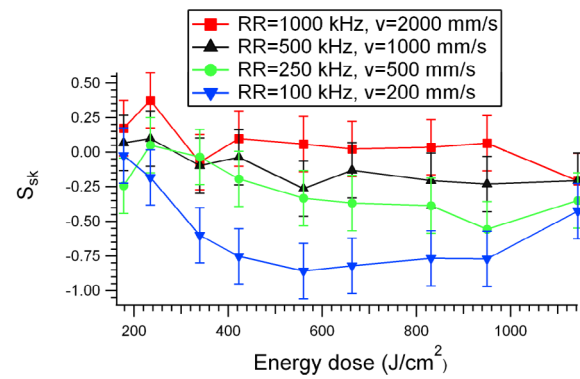

Figure 6. Evolution of the RMS roughness S_q with energy dose E for ultrashort laser-textured surfaces (evaluation area: $336 \times 336 \ \mu\text{m}^2$). The error bars associated with the values of E are the same size as the markers (standard deviation).
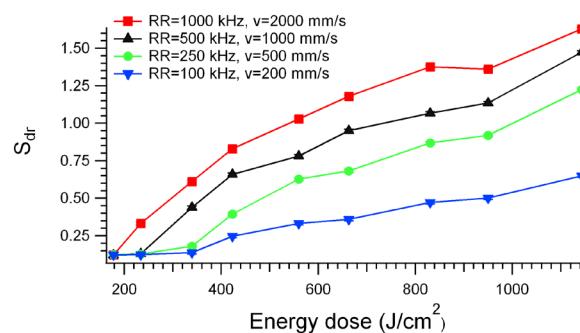

Figure 7. Evolution of the skewness S_{sk} with energy dose E for ultrashort laser-textured surfaces (evaluation area: $336 \times 336 \ \mu\text{m}^2$). The error bars associated with the values of E are the same size as the markers (standard deviation).

Figure 8. Evolution of the developed area ratio S_{dr} with energy dose E for ultrashort laser-textured surfaces (evaluation area: $336 \times 336 \ \mu\text{m}^2$). The error bars associated with the values of E and S_{dr} are the same size as the markers (standard deviation).
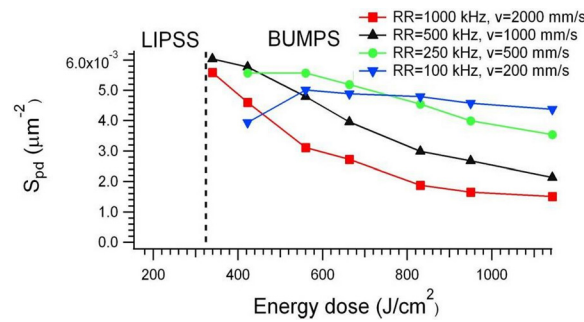
Figure 9. Evolution of the density of peaks S_{pd} with energy dose E for ultrashort laser-textured surfaces (evaluation area: 336×336 μm^2). The dashed vertical line represents a a qualitative estimate of the value of E at which a transition between bumps and LIPSS occurs. The error bars associated with the values of E are the same size as the markers (standard deviation).
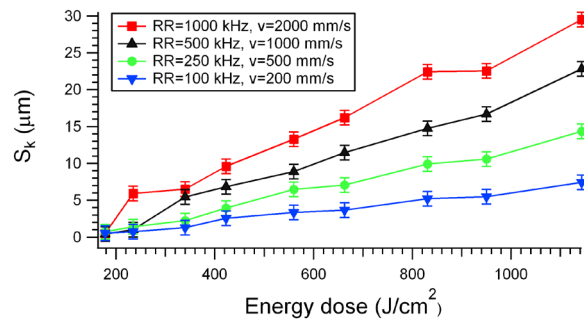

Figure 10. Evolution of the core roughness S_k with energy dose E for ultrashort laser-textured surfaces (evaluation area: 336×336 μm^2). The error bars associated with the values of E are the same size as the markers (standard deviation).

With regards to the behaviour of S_{dr}, a strong correlation between this parameter and E was observed. In particular, an increasing level with E, similar to that found for S_a and S_q, was observed. The S_{dr} parameter takes account of the ratio between the actual surface area and the projected measurment area (for further information, see the appendix). Therefore, it can be seen that the ablation process increases the total interfacial area with energy doses. According to some studies on the influence of surface roughness on bacterial adhesion [24], an increase in the interfacial area is not necessarily reflected in an increase in the surface available for cellular attachment. In particular, as we pointed out in section 2, large areas could trap air bubbles, thus hindering cellular adhesion. Further investigations on bacterial attachment should be performed in order to clarify this point.

In figure 9, the density of peaks S_{pd} is plotted versus the quantity E. First of all, we note that the reported curves, corresponding to fixed values of RR, have a well-defined behaviour for high energy doses, in accordance with the qualitative observation of SEM and interferometric data. In particular, for fixed RR, S_{pd} decreases with increasing E, with a rate depending on the repetition rate, indicating an increase in the overall size of the surface structures. In addition, a decrease in RR at fixed E leads to textures with denser peaks with greater values of S_{pd}. This trend confirms the qualitative observations made on the interferometric maps. For decreasing energy doses, the limits in the resolution of the coherence scanning interferometer become more and more evident. In particular, the calculation of S_{pd} is heavily affected by the occurrence of the transition between bumps and LIPSS, represented approximately by the dashed vertical line in figure 9. Another crucial point is that none of the surfaces examined here seem to match the condition on the values of S_{pd} defined in section 2. However, peaks of sizes 1–1.5 μm are distinguishable in the SEM images (figure 3 for $E = 178.0$ J cm^{-2}). Such peaks either cannot be resolved in the interferometric maps, or they are excluded from the counting of peaks by the procedure for the calculation of S_{pd} dictated by the ISO standard. Moreover, SEM images obtained with a higher resolution show that all the surfaces present a hierarchical shape. Therefore, additional investigations on the S_{pd} parameter with microscopies that allow us to resolve sub-micrometric features and concrete tests on bacterial adhesion are needed in order to clarify this point. In addition, we cannot exclude the effects of the extracellular polymeric substance or of the cell curvature that should, in principle, relax the requirements made here.

In figures 10–12 the parameters S_k, S_{pk} and S_{vk} as a function of E are shown. All the parameters demonstrate an increasing behaviour with increasing values of E with a growth rate that decreases with a decrease in RR. This behaviour is more evident with the S_k parameter related to the depth of the core roughness. The behaviour of S_k is similar to that of S_a and S_a since S_k measures an amplitude property.
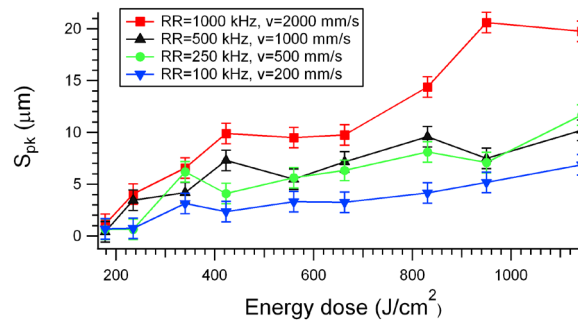
Figure 11. Evolution of the reduced peak height S_{pk} with energy dose E for ultrashort laser-textured surfaces (evaluation area: $336 \times 336 \ \mu m^2$). The error bars associated with the values of E are the same size as the markers (standard deviation).
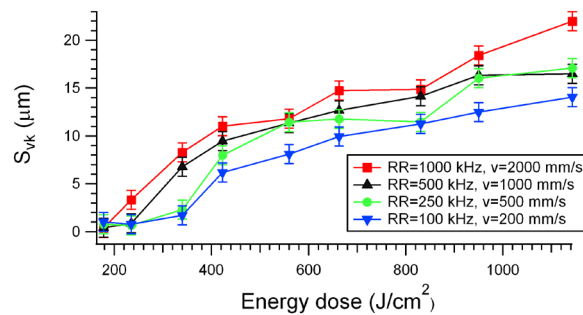

Figure 12. Evolution of the reduced valley depth S_{vk} with energy dose E for ultrashort laser-textured surfaces (evaluation area: $336 \times 336 \ \mu m^2$). The error bars associated with the values of E are the same size as the markers.

According to the definitions of S_{pk} and S_{vk}, the graphs observed in figures 11 and 12 show that an increase in E causes an increase in the depth of the highest peaks (S_{pk} versus E) and an increase in the depth of the deepest dales (S_{vk} versus E). However, S_{pk} seems to be more sensitive to the choice of RR than S_{vk}.

6. Further development

According to the main theories on the correlation between surface roughness and cellular adhesion, outlined in section 2, the laser treatments regarding the surfaces obtained at energy doses greater than 235 J cm^{-2} seem to be unsuitable for the realization of antibacterial surfaces, i.e. do not satisfy the condition outlined in section 2 for antibacterial surfaces. Unfortunately, the resolution of the coherence scanning interferometer employed to perform the topographical analysis of the surfaces did not allow full resolution of the surface structures obtained at energy doses less than 235 J cm^{-2}. Further investigations are needed in order to obtain topographical maps with better resolution. Furthermore, concrete measurements of bacterial attachment have to be performed in order to assess whether these surfaces are antibacterial with respect to the non-treated substrate, and to quantify whether the amount of biofilm is correlated with the specific processing conditions. In addition, it would be interesting to verify which parts of the surface texture bacterial cells adhere preferentially in order to establish whether the conditions defined in section 2, based on the so-called 'sheltering effect', and on the contact area between a single cell and the substratum, are correct. However, the general conclusion that can be drawn from the overall topographical analysis is that structures with smaller and denser surface structures have to be realized in order to reach the size of bacterial cells. This aim could be achieved with two strategies. Firstly, one of the advantages of ultrashort laser treatment is the possibility of obtaining hierarchical surface structures with a relatively low number of pulses. Therefore, for laser fluences well above the ablation threshold, a reduction in the number of passes supplied to the target could reduce the risk of partially canceling the structures created by the first pulses. Secondly, according to the main theories on the formation of LIPSS [25], smaller structures could be obtained with lower wavelengths, e.g. by working in the UV spectrum. Another open point is the influence of the surface chemistry induced by the laser processing on the bacterial attachment. The laser treatment induces the formation of a layer of oxide [54]. However, it is not clear how the interaction between this layer and the cell wall or the extracellular polymeric substance influences bacterial adhesion. Therefore, further investigations on the chemical nature of the surfaces

realized, e.g. XPS spectrometry, could be useful to clarify this point.

7. Conclusions

In this work, a detailed characterization of the surface morphology of stainless steel surfaces textured by an ultrashort pulsed laser was performed. The metrological parameters employed have been calculated within the framework of the standard ISO 25178. It is evident, however, that laser ablation increases the global level of roughness as a function of energy dose E. This trend means that there is an increase in the average height of surface structures, evident in the behaviour of S_a and S_q, an increase in the average peak spacing, as shown in the behaviour of S_{pd}, and an increase in the core height, as shown by S_k, when the energy dose delivered to the surface increases. The calculation performed also indicates that S_{sk} is less easy to control by acting on the laser parameters. However, the substantial behaviour of such a parameter indicates that laser ablation increases the fraction of the surface occupied by dales over the fraction occupied by peaks. The S_{dr} parameter reveals that, for growing energy doses, the total surface area increases due to the ablation process. As pointed out in section 5, we cannot yet establish if this property is deleterious in the attempt to realize an anti-biofouling surface. In particular, further investigations on the power of trapping air bubbles and experiments on bacterial adhesion are needed in order to clarify this point. Finally, the parameters S_{pk} and S_{vk} demonstrate that an increase in the structure size corresponds to a relative decrease in the average height of the peaks and dales. In addition, it was ascertained that none of the surfaces examined seem to match the conditions of S_{pd} defined to grant an anti-biofouling property, at least from the measurement defined so far. Furthermore, the values of S_a observed in almost all the surfaces analyzed are far greater than the thresholds of those normally indicated in the commonly adopted ISO norms for hygienic surfaces specified in section 2. However, it is expected that sub-micrometric features characterizing surface textures realized with ultrashort laser treatment should lead to higher values of S_{pd} approaching the requested value of four peaks per squared micron. Analyses of biofilm formation will be performed on larger areas textured with the parameter combinations hypothesized in this work in order to clarify if the guidelines for the surface design are sufficient for the preliminary planning of anti-adhesion functionalities for healthcare applications.

Appendix. Definitions of areal surface parameters

In the following, metrological parameters employed to decribe the topography of the surfaces characterized in this article will be described. As already mentioned, all the parameters are included in the standard ISO 25178. The correlation to the amount of cellular adhesion has already been observed for some of the parameters presented here [55–58], while for the others this correlation must be verified with experimental observations.

The topographical information consists of a real matrix, whose elements $\{z_{i,j}\}$, with $i = 1,\ldots,N_x$, $j = 1,\ldots,N_y$, represent the local height with respect to the average plane.

The most commonly adopted parameter to characterize the global level of roughness is the so-called *average roughness* S_a, defined as

$$S_a = \frac{1}{N_x N_y} \sum_{i=1}^{N_x} \sum_{j=1}^{N_y} |z_{i,j}|. \tag{A1}$$

Another widespread roughness parameter is the *RMS roughness* S_q, defined as

$$S_q = \sqrt{\frac{1}{N_x N_y} \sum_{i=1}^{N_x} \sum_{j=1}^{N_y} z_{i,j}^2}. \tag{A2}$$

Despite the fact that both S_a and S_q give a measure of the average deviation of the surface topography from the mean line of the mean plane, the RMS roughness is considered to be more meaningful than the average roughness because it represents the standard deviation of the distribution of heights.

It is common for two surfaces with clearly different structures to have similar values of S_a and S_q [38]. Therefore, the description of surface topography is usually enriched by introducing moments of the height distribution of successive orders, in particular, skewness S_{sk} and kurtosis S_{ku} [59]. However, in this work, S_{ku} has been found to be weakly corrrelated with the processing parameters. For this reason, in this analysis, S_{ku} has been neglected.

The *skewness* parameter is defined as the moment of the 3rd order of the distribution of heights, and it is given by

$$S_{sk} = \frac{1}{S_q^3 N_x N_y} \sum_{i=1}^{N_x} \sum_{j=1}^{N_y} z_{i,j}^3. \tag{A3}$$

Skewness quantifies the asymmetry of the distribution of heights with respect to the mean value. In particular, $S_{sk} > 0$ indicates a dominance in peaks over valleys, while $S_{sk} < 0$ indicates a dominance in valleys over peaks.
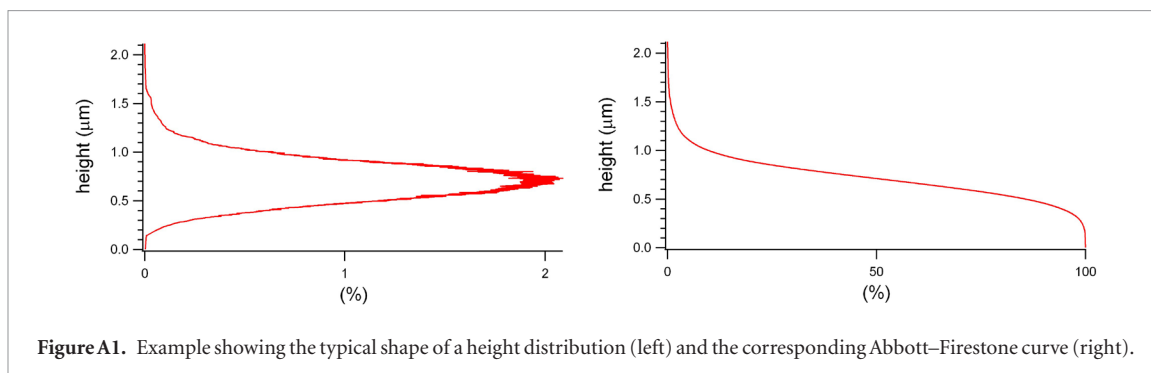
Figure A1. Example showing the typical shape of a height distribution (left) and the corresponding Abbott–Firestone curve (right).
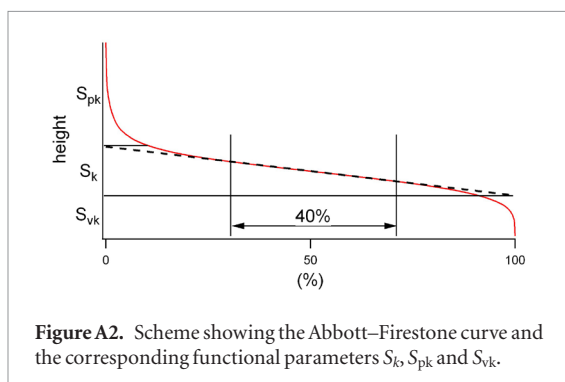

Figure A2. Scheme showing the Abbott–Firestone curve and the corresponding functional parameters S_k, S_{pk} and S_{vk}.

One of the most relvant effects of laser treatment is the increase of the total interfacial area. To quantify this increase, the *developed area ratio* S_{dr} has been introduced. It is defined as

$$S_{dr} = \frac{A_{interf} - A}{A} \tag{A4}$$

where A_{interf} is the total interface area, calculated with a process of triangulation, while A is the projection of A_{interf} on the mean plane. In other words, this dimensionless parameter increases with an increase in the interfacial area.

The *density of peaks* S_{pd} is the number of peaks per unit of surface. One of the most relevant problems regarding the calculation of such a parameter is the tendency to overestimate the number of hills, and, therefore, the value of S_{pd}. According to the ISO standard employed, the S_{pd} parameter was calculated on the filtered maps by applying, in sequence, the watershed algorithm on the topographical map multiplied by -1, in order to segment the hills, and a Wolf pruning algorithm of 0.2 μm in order to exclude non-significant peaks from the density calculations [27]. In particular, due to the limits in the resolution specified in section 5, the surface analysis was limited to micrometric motifs. All the calculations were performed on an evaluation area of 336×336 μm^2. This area was judged large enough to ensure a statistical significance to the calculations.

Finally, the so-called functional parameters, the *core roughness* S_k, the *reduced peak height* S_{pk} and the *reduced valley depth* S_{vk} have been analyzed. These parameters are derived from the so-called *Abbott–Firestone curve*, defined as the integral of the distribution of heights (see figure A1).

According to the ISO 12178 standard, the three functional parameters studied in this work have been determined by considering the secant to the Abbott–Firestone curve, passing through the points corresponding to the value of 0% and 40% on the horizontal axis. The procedure consists of translating these two points along the horizontal axis by maintaining the horizontal relative distance of 40% until the absolute value of the slope of the secant to the curve reaches a minimum [60]. This final situation is represented by the dashed line shown in the scheme in figure A2.

At this point, the functional parameters S_k, S_{pk} and S_{vk} are defined as the lengths shown in figure A2.

ORCID iDs

L Romoli ⓘ https://orcid.org/0000-0003-3918-4276

References

[1] Liu K and Jiang L 2011 Bio-inspired design of multiscale structures for function integration *Nano Today* **6** 155

[2] Bhushan B 2016 *Biomimetics: Bioinspired Hierarchical-Structured Surfaces for Green Science and Technology* (Berlin: Springer)

[3] Bhushan B 2009 Biomimetics: lessons from nature—an overview *Phil. Trans. R. Soc.* A **367** 1445

[4] Aizenberg J and Fratzl P 2009 Biological and biomimetic materials *Adv. Mater.* **21** 387

[5] Yao X, Song Y and Jiang L 2011 Applications of bio-inspired special wettable surfaces *Adv. Mater.* **23** 387

[6] Kumar C G and Anand S K 1998 Significance of microbial biofilms in food industry: a review *Int. J. Food Microbiol.* **42** 9

[7] Katsikogianni M and Missirlis Y F 2004 Concise review of mechanisms of bacterial adhesion to biomaterials and of techniques used in estimating bacteria-material interactions *Eur. Cell Mater.* **8** 37

[8] Teh K H, Flint S, Brooks J and Knight G 2015 *Biofilms in the Dairy Industry* (New York: Wiley)

[9] Xia F and Jiang L 2008 Bio-inspired, smart, multiscale interfacial materials *Adv. Mater.* **20** 2842

[10] Chen F, Zhang D, Yang Q, Yong J, Du G, Si J, Yun F and Hou X 2013 Bioinspired wetting surface via laser microfabrication *ACS Appl. Mater. Interfaces* **5** 6777

[11] Bhushan B and Jung Y C 2007 Wetting study of patterned surfaces for superhydrophobicity *Ultramicroscopy* **107** 1033

[12] Wu D, Wang J, Wu S, Chen Q, Zhao S, Zhang H, Sun H and Jiang L 2011 Three-level biomimetic rice-leaf surfaces with controllable anisotropic sliding *Adv. Funct. Mater.* **21** 2927

[13] Ko D, Tumbleston J R, Henderson K J, Euliss L E, DeSimone J M, Lopez R and Samulski E T 2011 Biomimetic microlens array with antireflective 'moth-eye' surface *Soft. Matter.* **7** 6404

[14] Leem J W, Guan X, Choi M and Yu J S 2015 Broadband and omnidirectional highly-transparent coverglasses coated with biomimetic moth-eye nanopatterned polymer films for solar photovoltaic system applications *Sol. Energy Mater. Sol. Cells* **134** 45

[15] Lee H, Lee B P and Messersmith P B 2007 A reversible wet/dry adhesive inspired by mussels and geckos *Nature* **448** 338

[16] Feng J, Tuominen M T and Rothstein J P 2011 Hierarchical superhydrophobic surfaces fabricated by dual-scale electron-beam-lithography with well-ordered secondary nanostructures *Adv. Funct. Mater.* **126** 62

[17] Peng S, Tian D, Yang X and Deng W 2014 Highly efficient and large-scale fabrication of superhydrophobic alumina surface with strong stability based on self-congregated alumina nanowires *Appl. Mater. Interfaces* **6** 4831

[18] Zhang B T, Liu B L, Deng X B, Cao S S, Hou X H and Chen H L 2008 Fabricating superhydrophobic surfaces by molecular accumulation of polysiloxane on the wool textile finishing *Colloid Polym. Sci.* **286** 453

[19] Lu X Y, Zhang J L, Zhang C C and Han Y C 2005 Low-density polyethylene (LDPE) surface with a wettability gradient by tuning its microstructures *Macromol. Rapid. Commun.* **26** 637

[20] Giljean S, Bigerelle M, Anselme K and Haidara H 2011 New insights on contact angle/roughness dependence on high surface energy materials *Appl. Surf. Sci.* **257** 9631

[21] Manca M, Cannavale A, De Marco L, Arico A S, Cingolani R and Gigli G 2009 Durable superhydrophobic and antireflective surfaces by trimethylsilanized silica nanoparticles-based sol–gel processing *Langmuir* **25** 6357

[22] Taurino R, Fabbri E, Messori M, Pilati F, Pospiech D and Synytska A 2008 Facile preparation of superhydrophobic coatings by sol–gel processes *J. Colloid Interface Sci.* **325** 149

[23] Fadeeva E, Truong V K, Stiesch M, Chichkov B N, Crawford R J, Wang J and Ivanova E P 2011 Bacterial retention on superhydrophobic titanium surfaces fabricated by femtosecond laser ablation *Langmuir* **27** 3012

[24] Truong V K, Webb H K, Fadeeva E, Chichkov B N, Wu A H F, Lamb R, Wang J Y, Crawford R J and Ivanova E P 2012 Air-directed attachment of coccoid bacteria to the surface of superhydrophobic lotus-like titanium *Biofouling* **28** 539

[25] Ahmmed K M T, Grambow C and Kietzig A 2014 Fabrication of micro/nano structures on metals by femtosecond laser micromachining *Micromachines* **5** 1219

[26] Jiang X, Scott P J, Whitehouse D J and Blunt L 2007 Paradigm shifts in surface metrology. Part II. The current shift *Proc. R. Soc.* A **463** 2071

[27] Leach R 2013 Introduction to surface topography *Characterisation of Areal Surface Texture* (Berlin: Springer)

[28] Suh A Y, Polycarpou A A and Conry T F 2003 Detailed surface roughness characterization of engineering surfaces undergoing tribological testing leading to scuffing *Wear* **255** 556

[29] Goodhand M N, Walton K, Blunt L, Lung H W, Miller R J and Marsden R 2016 The limitations of using 'R_a' to describe surface roughness *J. Turbomach.* **138** 101003

[30] Jullien C, Bénézech T, Carpentier B, Lebret V and Faille C 2003 Identification of surface characteristics relevant to the hygienic status of stainless steel for the food industry *J. Food Eng.* **56** 77

[31] Faille C, Membre J M, Ussier J P, Bellon-Fontaine M N, Carpentier B, Laroche M A and Benezech T 2000 Influence of physicochemical properties on the hygienic status of stainless steel with various finishes *Biofouling* **15** 261

[32] Leclercq-Perlat M N and Lalande M 1994 Cleanability in relation to surface chemical composition and surface finishing of some materials commonly used in food industries *J. Food Eng.* **23** 501

[33] Wirtanen G, Ahola H and Mattila-Sandholm T 1995 Evaluation of cleaning procedures for elimination of biofilm from stainless steel surfaces in open process equipment *Food Bioprod. Process.* **73** 9–16

[34] Barnes L M, Lo M F, Adams M R and Chamberlain A H L 1999 Effect of milk proteins on adhesion of bacteria to stainless steel surfaces *Appl. Environ. Microbiol.* **65** 4543

[35] Wang X, Li Y, Onnis-Hayden A, Gao C, Gu A Z and Wan K T 2012 Correlation of macroscopic aggregation behavior and microscopic adhesion properties of bacteria strains using a dimensionless Tabor's parameter *J. Colloid Interface Sci.* **374** 70

[36] Wang X, Li Y, Gu A Z and Wan K T 2013 Predicting macroscopic colloidal deposition and transportation based on dimensionless Tabor's parameter *Nano Life* **3** 1340009

[37] Li Y, Wang X, Onnis-Hayden A, Wan K T and Gu A Z 2014 Universal quantifier derived from AFM analysis links cellular mechanical properties and cell–surface integration forces with microbial deposition and transport behavior *Environ. Sci. Technol.* **48** 1769

[38] Crawford R J, Webb H K, Truong V K, Hasan J and Ivanova E P 2012 Surface topographical factors influencing bacterial attachment *Adv. Colloid Interface Sci.* **179** 142

[39] Scheuerman T R, Camper A K and Hamilton M A 1998 Effects of substratum topography on bacterial adhesion *J. Colloid Interface Sci.* **208** 23

[40] Verran J and Maryan C J 1997 Retention of *Candida albicans* on acrylic resin and silicone of different surface topography *J. Prosthet. Dent.* **77** 535

[41] Whitehead K A, Colligon J and Verran J 2005 Retention of microbial cells in substratum surface features of micrometer and sub-micrometer dimensions *Colloids Surf.* B **41** 129

[42] Ivanova E P, Truong V K, Webb H K, Baulin V A, Wang J Y, Mohammodi N, Wang F, Fluke C and Crawford R J 2011 Differential attraction and repulsion of *Staphylococcus aureus* and *Pseudomonas aeruginosa* on molecularly smooth titanium films *Sci. Rep.* **1** 165

[43] Verran J, Packer A, Kelly P and Whitehead K A 2010 The retention of bacteria on hygienic surfaces presenting scratches of microbial dimensions *Lett. Appl. Microbiol.* **50** 258

[44] Lorenzetti M, Dogša I, Stošvicki T, Stopar D, Kalin M, Kobe S and Novak S 2015 The influence of surface modification on bacterial adhesion to titanium-based substrates *ACS Appl. Mater. Interfaces* **7** 1644

[45] Bollen C M, Lambrechts P and Quirynen M 1997 Comparison of surface roughness of oral hard materials to the threshold surface roughness for bacterial plaque retention: a review of the literature *Dent. Mater.* **13** 258

[46] Scardino A J, Harvey E and De Nys R 2006 Testing attachment point theory: diatom attachment on microtextured polyimide biomimics *Biofouling* **22** 55

[47] Mincuzzi G, Gemini L, Faucon M and Kling R 2016 Extending ultra-short pulse laser texturing over large area *Appl. Surf. Sci.* **386** 65

[48] Gemini L, Hashida M, Shimizu M, Miyazaka Y, Inoue S, Tokita S, Limpouch J, Mocek T and Sakabe S 2013 Metal-like self-organization of periodic nanostructures on silicon and silicon carbide under femtosecond laser pulses *J. Appl. Phys.* **114** 194903

[49] Bonse J, Krüger J, Höhm S and Rosenfeld A 2012 Femtosecond laser-induced periodic surface structures *J. Laser Appl.* **24** 042006

[50] Bonse J, Hohm S, Kirner S V, Rosenfeld A and Kruger J 2017 Laser-induced periodic surface structures—A scientific evergreen *IEEE J. Sel. Top. Quantum Electron.* **23** 9000615

[51] Tsibidis G D, Fotakis C and Stratakis E 2015 From ripples to spikes: a hydrodynamical mechanism to interpret femtosecond laser-induced self-assembled structures *Phys. Rev.* B **92** 041405

[52] Gadelmawla E S, Koura M M, Maksoud T M A, Elewa I M and Soliman H H 2002 Roughness parameters *J. Mater. Process. Technol.* **123** 133

[53] Neuenschwander B, Jaeggi B, Schmid M, Rouffiange V and Martin P E 2012 Optimization of the volume ablation rate for metals at different laser pulse-durations from ps to fs *Proc. SPIE* **8243** 824307

[54] Kietzig A M, Hatzikiriakos S G and Englezos P 2009 Patterned superhydrophobic metallic surfaces *Langmuir* **25** 4821

[55] Kathiresan S and Mohan B 2017 *In vitro* bacterial adhesion study on stainless steel 316L subjected to magneto rheological abrasive flow finishing *Biomed. Res.* **28** 7

[56] Rochford E T J, Poulsson A H C, Varela J S, Lezuo P, Richards R G and Moriarty T F 2014 Bacterial adhesion to orthopaedic implant materials and a novel oxygen plasma modified PEEK surface *Colloids Surf.* B **113** 213

[57] Zhao Q, Liu Y, Wang C, Wang S, Peng N and Jeynes C 2008 Reduction of bacterial adhesion on ion-implanted stainless steel surfaces *Med. Eng. Phys.* **30** 341

[58] Shaikh S, Singh D, Subramanian M, Kedia S, Singh A K, Singh K, Gupta N and Sinha S 2017 Femtosecond laser induced surface modification for prevention of bacterial adhesion on 45S5 bioactive glass in preparation (arXiv:1706.06327)

[59] Thomas T R 1999 *Rough surfaces* (London: Imperial College Press)

[60] Blunt L and Jiang X 2003 *Advanced Techniques for Assessment Surface Topography: Development of a Basis for 3D Surface Texture Standards 'Surfstand'* (Amsterdam: Elsevier)